

Article

Tailoring the Composition of Ba_xBO_3 (B = Fe, Mn) Mixed Oxides as CO or Soot Oxidation Catalysts in Simulated GDI Engine Exhaust Conditions

Álvaro Díaz-Verde , Salvador Montilla-Verdú, Verónica Torregrosa-Rivero  and María-José Illán-Gómez * 

Carbon Materials and Environment Research Group, Inorganic Chemistry Department, University of Alicante, 03690 Alicante, Spain; alvaro.diaz@ua.es (Á.D.-V.); salvador.montilla@ua.es (S.M.-V.);

vero.torregrosa@ua.es (V.T.-R.)

* Correspondence: illan@ua.es

Abstract: Mixed oxides with perovskite-type structure (ABO_3) are promising catalysts for atmospheric pollution control due to their interesting and tunable physicochemical properties. In this work, two series of Ba_xMnO_3 and Ba_xFeO_3 ($x = 1$ and 0.7) catalysts were synthesized using the sol-gel method adapted to aqueous medium. The samples were characterized by μ -XRF, XRD, FT-IR, XPS, H_2 -TPR, and O_2 -TPD. The catalytic activity for CO and GDI soot oxidation was determined by temperature-programmed reaction experiments (CO-TPR and soot-TPR, respectively). The results reveal that a decrease in the Ba content improved the catalytic performance of both catalysts, as B0.7M-E is more active than BM-E for CO oxidation, and B0.7F-E presents higher activity than BF for soot conversion in simulated GDI engine exhaust conditions. Manganese-based perovskites (BM-E and B0.7M-E) achieve better catalytic performance than iron-based perovskite (BF) for CO oxidation reaction due to the higher generation of active sites.

Keywords: perovskite; iron; manganese; CO oxidation; GDI soot oxidation



Citation: Díaz-Verde, Á.;

Montilla-Verdú, S.; Torregrosa-Rivero,

V.; Illán-Gómez, M.-J. Tailoring the

Composition of Ba_xBO_3 (B = Fe, Mn)

Mixed Oxides as CO or Soot

Oxidation Catalysts in Simulated

GDI Engine Exhaust Conditions.

Molecules **2023**, *28*, 3327. [https://](https://doi.org/10.3390/molecules28083327)

doi.org/10.3390/molecules28083327

Academic Editors: Maxim

L. Kuznetsov, Barbara Bonelli and

Giorgio Vilardi

Received: 31 January 2023

Revised: 14 March 2023

Accepted: 7 April 2023

Published: 9 April 2023



Copyright: © 2023 by the authors.

Licensee MDPI, Basel, Switzerland.

This article is an open access article

distributed under the terms and

conditions of the Creative Commons

Attribution (CC BY) license ([https://](https://creativecommons.org/licenses/by/4.0/)

[creativecommons.org/licenses/by/](https://creativecommons.org/licenses/by/4.0/)

[4.0/](https://creativecommons.org/licenses/by/4.0/)).

1. Introduction

Currently, limitation of climate change is one of the most challenging topics due to its dangerous global effects on biological and human systems [1]. Greenhouse gases (GHGs), such as carbon dioxide, methane, and nitrogen oxides, are among the main species causing this problem. Since the industrial revolution, GHGs have been emitted into the atmosphere as the result of human activities, and their release has continuously increased [2]. The transport sector is the most responsible for GHG emissions, and predictions indicate that vehicles will contribute around 85% of the total GHGs emissions in 2040 if effective mitigation measures are not applied [3,4]. This scenario is pushing to the automotive industrial sector to use alternative systems to internal combustion engines, such as electric and fuel-cell-based engines [5–7]. However, nowadays, electric and fuel-cell-based vehicles are not as available as internal-combustion-engine-based vehicles due to their high economical costs, the limited number of available charging points, and their long charge times [8,9]. For this reason, internal combustion systems cannot be totally eliminated in the coming years, and consequently, additional measures to reduce the amount of pollutants emitted by these engines must continue to be implemented.

In addition to the GHGs, carbon monoxide (CO) and soot are considered dangerous pollutants, as they also increase morbidity rates. These chemical species, which are highlighted as hazardous emissions generated by gasoline direct injection (GDI) engines, have become more relevant in recent last years [10,11]. As GDI-engine-based vehicles offer a high fuel economy and reduced CO_2 emissions (compared to other gasoline engines), they were the most widely purchased passenger cars in 2017 [12].

The removal of these two pollutants is carried out using catalysts (three-way catalysts (TWCs) and gasoline particulate filters (GPF) units, respectively) that are able to convert these toxic substances into more benign ones. However, to comply with current and future legislation and due to the working conditions of current internal combustion engines, the development of a new generation of active phases for TWC and GPF units is a challenging task. These new active phases, among other characteristics, should present higher activities at lower temperatures than the current active phases. Noble-metal/ceria-based catalysts are proposed as promising materials for these applications due to the high oxygen storage capacity (OSC) and good redox properties of ceria-based support. However, these solids have limited use under real conditions, mainly due to the high cost of noble metals, (the amount of which should be minimized as much as possible [13–15]) and their low stability under working conditions for long periods of time [10]. In this sense, noble-metal-free catalysts, such as mixed oxides with perovskite-type structure (ABO_3) [16–20], have been proposed as an interesting family of catalysts combining tunable catalytic properties and low cost.

It is well known that the redox properties of the active phase of catalysts play an essential role in oxidation reactions, such as CO and soot. In fact, perovskites stand out because of their excellent redox properties, which are mainly determined by B cations. A problem associated with using noble-metal-based catalysts for CO oxidation is the inhibition caused by CO adsorption (which hinders the dissociative adsorption of O_2 [21]). In previous papers, manganese-based perovskite solids have been proposed as catalysts to be tested for CO oxidation [22–27]. Manganese is considered an essential component of CO oxidation catalysts, as its molecular orbitals have suitable energy for the adsorption and activation of CO and O_2 [22,23]. Moreover, the activity of CO oxidation is strongly correlated with Mn–O bond strength and increases as Mn–O bond strength decreases [22–24].

The CO oxidation mechanism has been widely studied, with researchers reporting that at temperatures below 300 °C, CO oxidation follows a suprafacial mechanism. Thus, the catalyst provides adsorption sites, exhibiting the appropriate electronic properties and symmetry to activate the reactants [23,25]. In fact, for transition-metal based catalysts, an Eley–Rideal mechanism has been proposed, whereby CO reduction takes place in the adsorbed states with dissociated adsorbed oxygen species [22,26,27]. At higher temperatures ($T > 300$ °C), the bulk lattice oxygen of the catalyst is involved in the reaction, so a Mars–Van–Krevelen redox mechanism takes place. Under such conditions, the consumed lattice oxygen is regenerated through the adsorption, dissociation, and incorporation of oxygen from the gas phase [23,25,28]. Moreover, it was found that the CO: O_2 ratio can promote a specific mechanism and that the kinetics of the reaction strongly depend on O_2 and CO concentrations [29], as well as on the amount of oxygen vacancies [22].

Considering this background, in order to study the CO oxidation reaction in this paper, two atmospheres were employed: (i) 0.1% CO—1% O_2 , which was selected to avoid competition for the catalyst active sites due to the low concentration of reactants, and (ii) 1% CO—1% O_2 , which was used as a closer approximation of the CO and O_2 concentrations in GDI exhaust.

On the other hand, it has been widely reported that soot oxidation can be catalyzed by O_2 , by NO, and by a mixture of them [27,30–32]. However, the composition of GDI exhaust is low in NO_x content, as fuel cuts (i.e., when the engine pumps air forms the intake to the exhaust [33,34]) are the only source of oxygen, most of which is used by the TWC unit. Therefore, a good catalyst for GDI soot oxidation should be able to adsorb oxygen in fuel-cut mode and to desorb it under regular operating conditions. Therefore, it is interesting to analyze soot oxidation under two different atmospheres: (i) in an inert atmosphere (He), simulating the regular operation conditions of a GDI engine, and (ii) in a slightly oxidant atmosphere (1% O_2 /He), which reproduces severe fuel-cut operation conditions, as well as the typical O_2 concentration at the turbine–GDI engine exit, i.e., upstream of the TWC [35].

Perovskite-based catalysts show a good oxygen storage capacity, since O_2 can be adsorbed and activated on the oxygen vacancies [30]. Therefore, $BaMnO_3$ solids have been used for GDI soot oxidation under the two different atmospheres indicated above [36], as well as for CO oxidation in simulated GDI exhaust engine conditions [37]. Additionally, we recently realized that the use of under-stoichiometric Ba_xMnO_3 perovskites improves the performance of raw $BaMnO_3$ for CO oxidation, showing that $Ba_{0.7}MnO_3$ formulation achieves the best results [38]. Based on this statement and the background described above for CO and soot oxidation, in this study, two series of $BaBO_3$ perovskite-type catalysts (with Ba_xMnO_3 and Ba_xFeO_3 formulation of $x = 1$ and 0.7 , respectively) were synthesized, characterized, and tested for CO and soot oxidation reactions as model reactions relevant for the potential use of these catalysts in the control of pollutants generated by GDI engines.

2. Results and Discussion

2.1. Chemical, Morphological, and Structural Characterization

X-Ray patterns for BM-E, B0.7M-E, BF, and B0.7F-E catalysts are shown in Figure 1a, and the corresponding BF-E and B0.7F samples are presented in Figure 1b. The corresponding XRD data are included in Table 1.

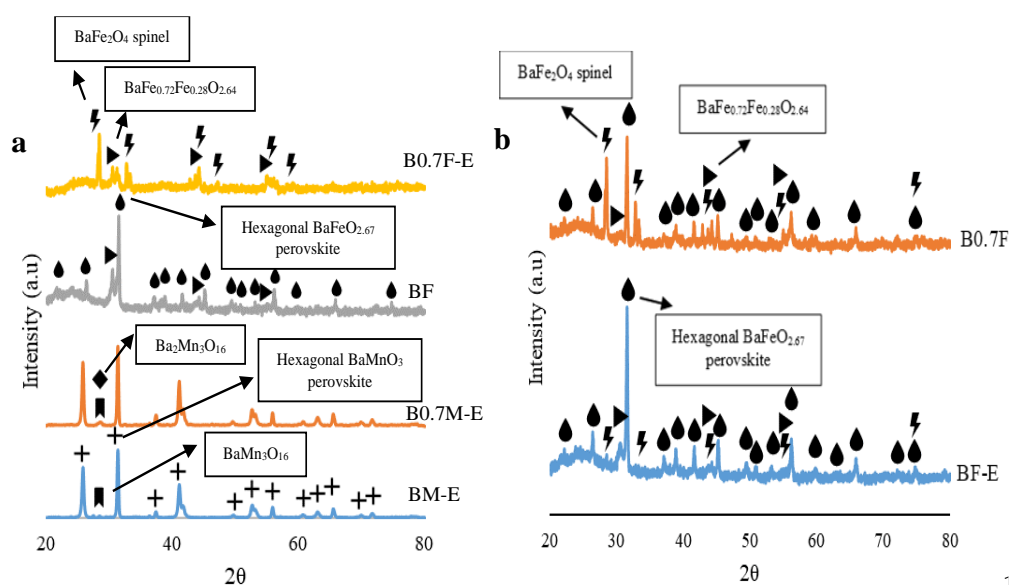


Figure 1. XRD patterns of (a) BM-E, B0.7M-E, BF, and B0.7F-E; and (b) BF-E and B0.7F catalysts.

Table 1. XRD data for BM-E, B0.7M-E, BF, and B0.7F-E catalysts.

Catalyst	Average Crystal Size (nm) ¹	Cell Parameters (Å)		
		a	b	c
BM-E	24.76	5.69	5.69	4.81
B0.7M-E	18.24	5.69	5.69	4.81
BF	49.52	5.67	5.67	13.96
B0.7F-E	23.09	19.02	5.38	8.48

¹ Average crystal sizes for the hexagonal perovskite phase, except for B0.7F-E, which corresponds to a spinel phase.

For manganese-based samples, BM-E and B0.7M-E catalysts exhibit a hexagonal $BaMnO_3$ perovskite structure ($a = b \neq c$) as the main crystalline phase, and $BaMn_3O_{16}$ and $Ba_2Mn_3O_{16}$ were detected as minority crystalline phases, appearing in very low amounts. The presence of these minority phases seems not to be related to the modification of the barium content, as a clear trend with barium content is not observed. Thus, the presence of these minority phases may be related to [39] (i) the formation of small precipitates during the gelation step, (ii) the use of a low calcination temperature, or (iii) a very short calcination

step. Note that the decrease in barium percentage does not generate significant structural modifications, since the cell parameters are not appreciably different (Table 1).

For iron-based samples, the BF diffractogram shows peaks corresponding to a hexagonal $\text{BaFeO}_{2.67}$ perovskite structure ($a = b \neq c$), while a peak associated with a BaFe_2O_4 orthorhombic spinel phase ($a \neq b \neq c$) was observed for the B0.7F-E catalyst. M. Sun et al. [40] suggested that the BaFe_2O_4 structure is formed when FeO_6 octahedrons of the perovskite lattice lose oxygen to form the FeO_4 tetrahedra present in the spinel lattice. Additionally, $\text{BaFe}_{0.72}\text{Fe}_{0.28}\text{O}_{2.64}$ mixed oxide (in which Fe(III) and Fe(IV) ions should coexist) was detected as a minority phase in both samples. In Figure 1b, it is observed that BF-E and B0.7F samples present a mixture of the three crystalline phases previously described for iron-based samples, that is, hexagonal $\text{BaFeO}_{2.67}$ perovskite, BaFe_2O_4 orthorhombic spinel, and $\text{BaFe}_{0.72}\text{Fe}_{0.28}\text{O}_{2.64}$; however, a predominant phase is not detected. Therefore, in order to simplify, only the samples presenting a clear main crystalline phase, that is, BM-E, B0.7M-E, BF, and B0.7F-E, were selected to carry out the activity studies.

For the selected catalysts, the average crystal size of the main crystalline phases was calculated by employing the Williamson–Hall method [41]; according to the results presented in Table 1, crystal growth is favored for stoichiometric perovskites, that is, for BM-E and BF.

In Table 2, the BET surface area (determined by N_2 adsorption) and the chemical bulk composition (both experimental and nominal values calculated using BaMnO_3 , $\text{Ba}_{0.7}\text{MnO}_3$, $\text{BaFeO}_{2.67}$, and BaFe_2O_4 formulae) are included for selected samples. Note that (i) all catalysts present a low surface area, as perovskite-type oxides are solids with negligible porosity [16,42–45], and (ii) the nominal and experimental bulk chemical compositions are similar, so the samples achieve the required weight percentages of Ba, Mn, Fe, or O.

Table 2. Chemical bulk composition and specific surface area data for BM-E, B0.7M-E, BF, and B0.7F-E catalysts.

Catalyst	BET Surface Area (m^2/g)	Chemical Composition (wt %)					
		Experimental			Nominal		
		Ba	Mn or Fe	O	Ba	Mn or Fe	O
BM-E	9	62	24	14	57	23	20
B0.7M-E	11	55	30	15	48	28	24
BF	9	59	24	17	58	24	18
B0.7F-E	10	51	30	19	44	36	20

FT-IR spectra of catalysts are shown in Figure 2. For the manganese-based samples, the following signals are observed: (i) stretching vibration of the Mn–O bonds in the MnO_6 octahedrons appears between 500 and 786 cm^{-1} , and (ii) asymmetric stretching of carbonate ions at 858 and 1443 cm^{-1} indicates the presence of BaCO_3 [46–48]. For iron-based samples, in addition to carbonate ions that, according to the intensity of signals, are present in a higher amount than in manganese-based samples, the following signals are located: (i) peaks at wavenumbers slightly higher than 598 and 665 cm^{-1} that correspond to the stretching vibration of the Fe–O bonds of FeO_6 octahedrons, indicating that the Fe–O bond is stronger than the Mn–O bond [49]; (ii) a signal placed at 768 cm^{-1} corresponding to a BaFe_2O_4 spinel, which is only detected for the B0.7F-E catalyst [49,50]; and (iii) a signal placed at 1060 cm^{-1} that corresponds to the stretching vibration of the C–OH bond [51–53]. The presence of carbon could be due to the remaining EDTA or citric acid, which was not completely removed during the calcination step. Note that as BaCO_3 was not detected by XRD, it should be an amorphous phase.

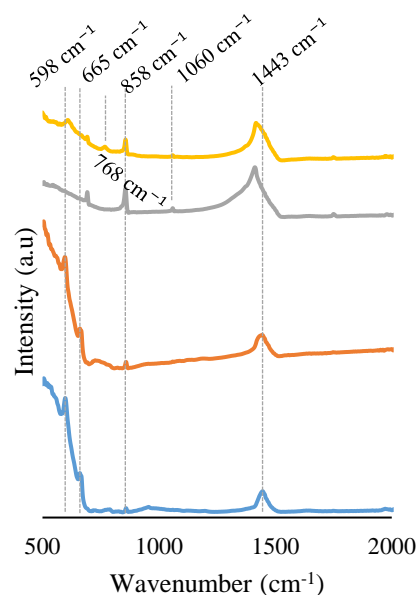


Figure 2. FT-IR spectra of BM-E, B0.7M-E, BF, and B0.7F-E catalysts.

2.2. Surface Properties

XPS spectra were obtained to determine the surface chemical composition of the selected samples. The spectra of the Ba $3d^{5/2}$ transition for both catalysts series shown in Figure 3 reveal that lattice Ba is the main species on the surface and that the amount of $BaCO_3$ (which was previously observed by FT-IR) is more abundant on the surface of iron-based catalysts than on manganese-based samples.

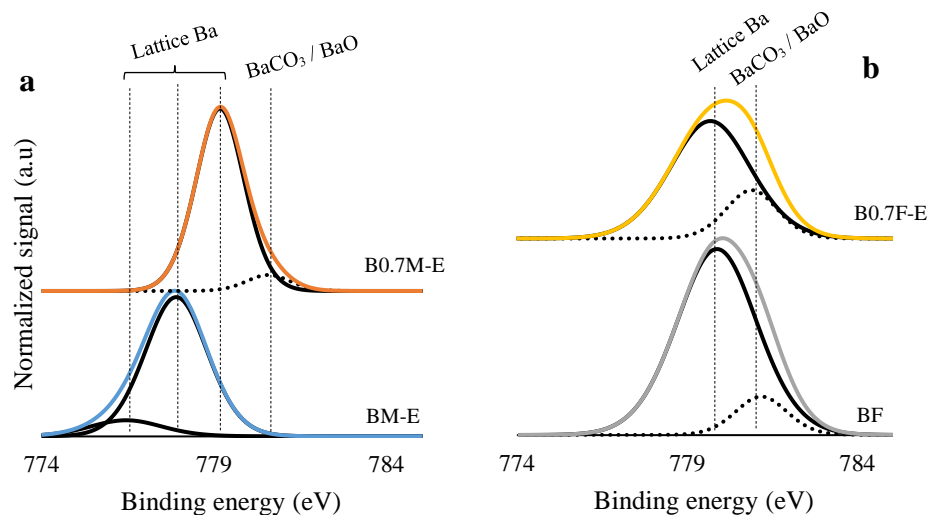


Figure 3. XPS spectra of the Ba $3d^{5/2}$ transition for BM-E and B0.7M-E (a) and for BF and B0.7F-E (b) catalysts.

XPS spectra corresponding to the Mn $2p^{3/2}$ transition are shown in Figure 4a. The registered signals are deconvoluted into two contributions associated with Mn(III) and Mn(IV), with Mn(III) located at lower binding energies than Mn(IV) [54]. The Mn(III)/Mn(IV) ratio values (presented in Table 3 and calculated by employing the corresponding area under the deconvoluted signals) reveal a higher amount of Mn(III) than of Mn(IV) on the catalyst surface and that the proportion of Mn(IV) increases as Ba content decreases. Thus, it seems that the oxidation of Mn(III) to Mn(IV) is the charge compensation mechanism working in this sample in order to counteract the decrease in the positive charge in barium-deficient perovskites [55].

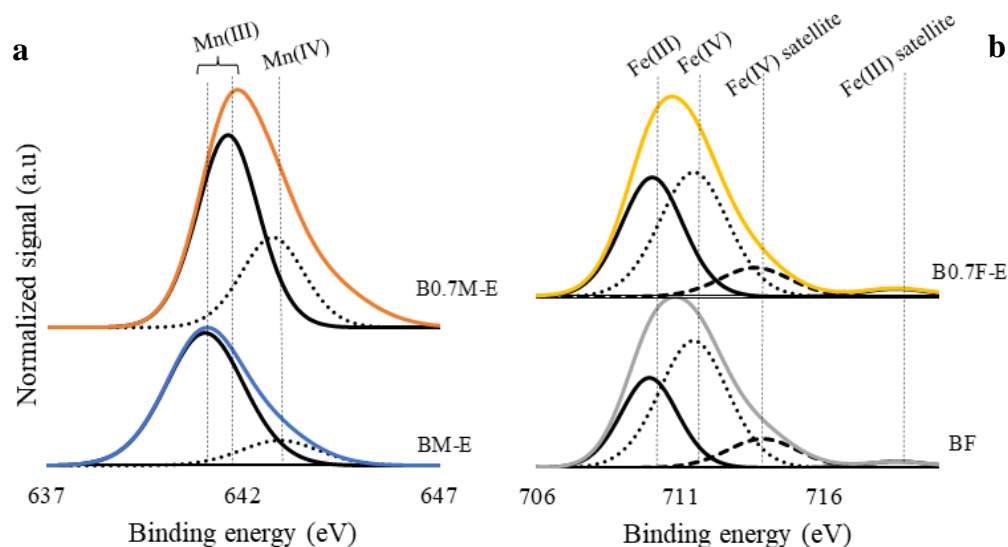


Figure 4. XPS spectra of the Mn $2p^{3/2}$ (a) and Fe $2p^{3/2}$ (b) transitions for BM-E, B0.7M-E, BF, and B0.7F-E catalysts.

Table 3. XPS data for BM-E, B0.7M-E, BF, and B0.7F-E catalysts.

Catalyst	Mn(III)/Mn(IV)	Fe(III)/Fe(IV)	XPS O_L /(Ba + Mn/Fe) (Nominal)
BM-E	5.3	-	1.2 (1.5)
B0.7M-E	2.1	-	1.2 (1.8)
BF	-	0.6	1.1 (1.5)
B0.7F-E	-	0.9	1.4 (1.3 ¹)

¹ Calculated based on the spinel formula ($BaFe_2O_4$).

In the Fe $2p^{3/2}$ transition spectra shown in Figure 4b, the following contributions can be identified: (i) an Fe(III) peak appearing at binding energies lower than those of Fe(IV) and (ii) Fe(IV) and Fe(III) satellite peaks located at approximately 713 eV and 718 eV, respectively [54,56,57]. The Fe(III)/Fe(IV) ratio values presented in Table 3 indicate that both Fe oxidation states coexist on the surface of the BF and B0.7F-E catalysts, with Fe(IV) as the main oxidation state for the two catalysts. However, as the Fe(III)/Fe(IV) ratio increases for B0.7F-E, the Fe(III) oxidation to Fe(IV) seems not to take place to compensate the positive charge deficiency as occurs for the B0.7M-E sample.

Finally, the deconvolution of the O 1s signal (Figure 5) shows three contributions: (i) a band located at binding energies around 529 eV, which is associated with the presence of lattice oxygen (O_L) [54,58]; (ii) a band located around 531 eV that is related to the existence of defects with low oxygen coordination, that is, the oxygen vacancies formed on the surface (O_{def}) [59]; (iii) a band detected at 532 eV that indicates the presence of adsorbed oxygen (O_{ads}), hydroxyl (-OH), and carbonate (CO_3^{2-}) groups on the catalyst surface [54,58,60]; and, finally, (iv) a band at approximately 533 eV corresponding to chemisorbed water (H_2O_{chem}) [61,62]. For iron-based samples (Figure 4b), lattice oxygen peak shows two contributions corresponding to the lattice oxygen of the two main crystalline phases detected by XRD ($BaFeO_{2.67}$ and $BaFe_2O_4$) at binding energies close to 531 eV and the oxygen of the $BaFe_{0.72}Fe_{0.28}O_{2.64}$ minority phase (observed in XRD) at binding energies of approximately 529 eV. Table 3 shows the experimental values of the O_L /(Ba + Mn/Fe) ratio (estimated using the areas under the corresponding deconvolutions) and the nominal values (calculated by employing the catalysts formulations of ABO_3 , $A_{0.7}BO_3$, or AB_2O_4). Thus, as the XPS ratios of BM-E, B0.7M-E, and BF are lower than the nominal ratios, the presence of oxygen vacancies on the surface of catalysts is featured. For manganese-based samples, the amount of oxygen vacancies increases as Ba content decreases, confirming the presence of a band corresponding to the oxygen defects (O_{def} , located at around 531 eV) in B0.7M-E. Thus, it

seems that the formation of these oxygen defects also enables counteracting the positive charge defect caused by the decrease in Ba content [63]. On the contrary, the formation of oxygen defects in the B0.7F-E sample is not promoted. Consequently, the change of structure from perovskite (in BF) to spinel (in B0.7F-E) seems to be the unique effect of Ba deficiency in iron-based catalysts.

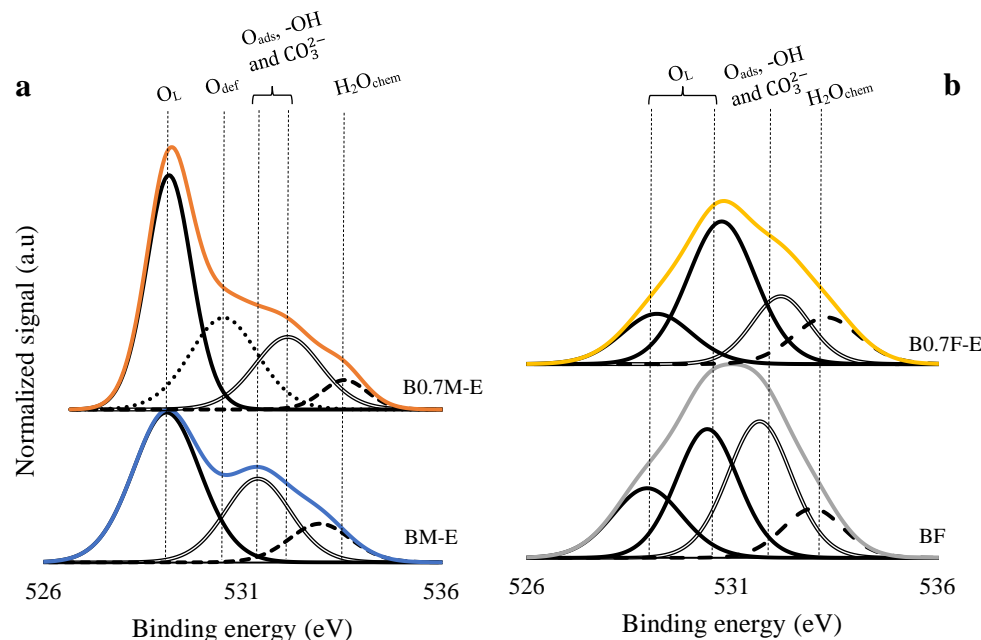


Figure 5. XPS spectra of the O 1s transition for BM-E and B0.7M-E (a) and for BF and B0.7F-E catalysts (b).

2.3. Redox Properties

Reducibility and redox properties of the catalysts were analyzed using temperature-programmed reduction with H_2 (H_2 -TPR), which represents the consumption profiles shown in Figure 6a.

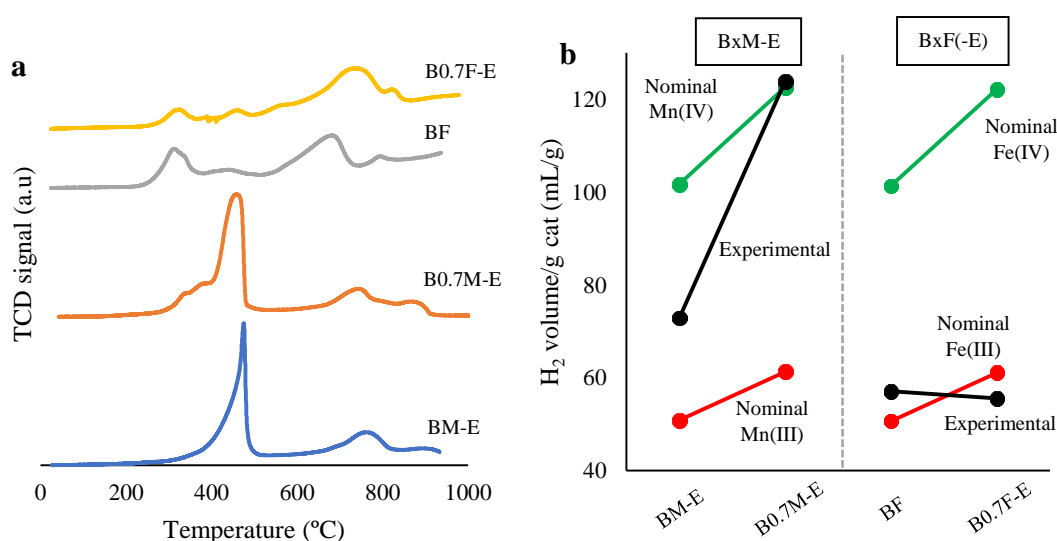


Figure 6. H_2 -TPR consumption profiles for catalysts (a) and H_2 consumption (mL/g of catalyst) (b).

For barium manganese-based samples, three different peaks are identified [36–38,64–68]: (i) a low-temperature peak, which appears between 400 °C and 500 °C, assigned to the reduction of Mn(IV) and Mn(III) to Mn(II); (ii) a low-intensity signal at temperatures

between 700 °C and 800 °C, which corresponds to the reduction of oxygen species on the catalysts surface; and (iii) another low-intensity band at around 900 °C due to the reduction of bulk Mn(III) to Mn(II). In the B0.7M-E sample, a small amount of hydrogen consumption is observed below 400 °C, which confirms the presence of Mn(IV) in the catalyst [69]. It is observed that the reduction of Mn(IV) and Mn(III) takes place at lower temperatures as the barium content decreases, probably due to a higher ionic mobility that improves the reduction process. This improved mobility has to be related to the presence of barium defects and oxygen vacancies in the structure [70].

On the other hand, for iron-based catalysts, the following peaks can be identified: (i) a peak at approximately 320 °C that corresponds to the reduction of Fe(IV) to Fe(III), (ii) a peak between 420 °C and 460 °C due to the partial reduction of Fe(III) to Fe(II), (iii) a third peak assigned to the reduction of the remaining Fe(III) between 650 °C and 740 °C, and finally, (iv) a peak at approximately 815 °C associated with the reduction of Fe(II) to Fe(0) [71]. It is observed that redox processes involving Fe cations take place at slightly lower temperatures in the BaFeO_{2.67} perovskite-type structure than in the BaFe₂O₄ spinel, which seems to be related to the higher amount of vacancies present in the oxygen-deficient perovskite than in the spinel structure, allowing a greater mobility and increased redox properties for the former.

In Figure 6b, the nominal and experimental consumptions of H₂ are compared for both series of catalysts. Nominal consumptions were calculated considering that manganese (either as Mn(III) or Mn(IV)) and iron (either as Fe(III) or Fe(IV)) are reduced to Mn(II) and Fe(0), respectively. Experimental values were calculated from the area under the H₂-TPR peaks identified in the H₂-TPR consumption profiles. For manganese-based catalysts, as the experimental consumption is closer to the nominal value corresponding to Mn(IV), it seems that Mn(III) and Mn(IV) species coexist in the bulk of catalysts, with Mn(IV) as the main oxidation state for the B0.7M-E catalyst. This is in agreement with the presence of a higher amount of Mn(IV) on the surface of this catalyst, as revealed by the Mn(III)/Mn(IV) XPS ratio (Table 3). Note that the higher H₂ consumption determined for the B0.7M-E catalyst with respect to the BM-E catalyst has to be also related to the higher amount of Mn present in this sample (see the chemical bulk composition in Table 2). However, as the normalized value of H₂ consumption (i.e., the percentage of Mn shown in Table 2) is still higher for B0.7M-E (4.2) than for BM-E (2.9), it seems to be confirmed that this sample presents a higher reducibility due to the presence of a higher amount of more reducible Mn(IV). On the other hand, for the iron-based samples, as the experimental values are closer to nominal Fe(III) values, the amount of Fe(III) in the catalysts bulk is higher than that of Fe(IV), as was also deduced by XPS (see the Fe(III)/Fe(IV) ratio in Table 3) for surface composition.

2.4. O₂ Release during Temperature-Programmed Desorption in He (O₂-TPD)

In the O₂-TPD profiles featured in Figure 7a, three different peaks can be identified [72,73]: (i) between 150 °C and 350 °C, corresponding to the desorption of the oxygen adsorbed on surface vacancies (called α -O₂); (ii) from 350 °C to 700 °C, the oxygen evolved comes from the adsorbed on the lattice defects (designated as α' -O₂); and (iii) above 700 °C, where the release of lattice oxygen (β -O₂) is detected. This β -oxygen is related to the reduction of Mn(IV)/Fe(IV) to Mn(III)/Fe(III) and the presence of oxygen vacancies in the bulk, which provides information about the oxygen mobility through perovskite lattice, which is a key factor determining the catalytic performance during oxidation reactions [74]. In Figure 7a, the total amount of desorbed oxygen and the weight loss percentage due to oxygen release for each catalyst are included.

Note that for manganese-based perovskites, the desorbed O₂ corresponds mainly to lattice oxygen (β -O₂), although the BM-E catalyst also presents a low α -O₂ emission and B0.7M-E shows a small O₂ desorption peak at around 600 °C. Furthermore, the amount of labile oxygen released is notably higher for the barium-deficient perovskite (B0.7M-E) than for BM-E because B0.7M-E presents a higher amount of Mn(IV) than BM-E. The high mobility of oxygen allows a greater reducibility of the catalysts, as shown by H₂-

TPR results (see Figure 6a) [73]. On the other hand, iron-based samples mainly evolve oxygen below 750 °C in the form of α -O₂ and α' -O₂ species [75]. Note that in this case, the sample evolving the highest amount of oxygen is the BF catalyst, as expected for an under-stoichiometric perovskite, which is the main crystalline phase for this sample (see Figure 1a). Note that the structural change from perovskite to spinel that occurs due to the decrease in barium content in B0.7F-E does not increase the amount of oxygen vacancies nor the amount of Fe(IV).

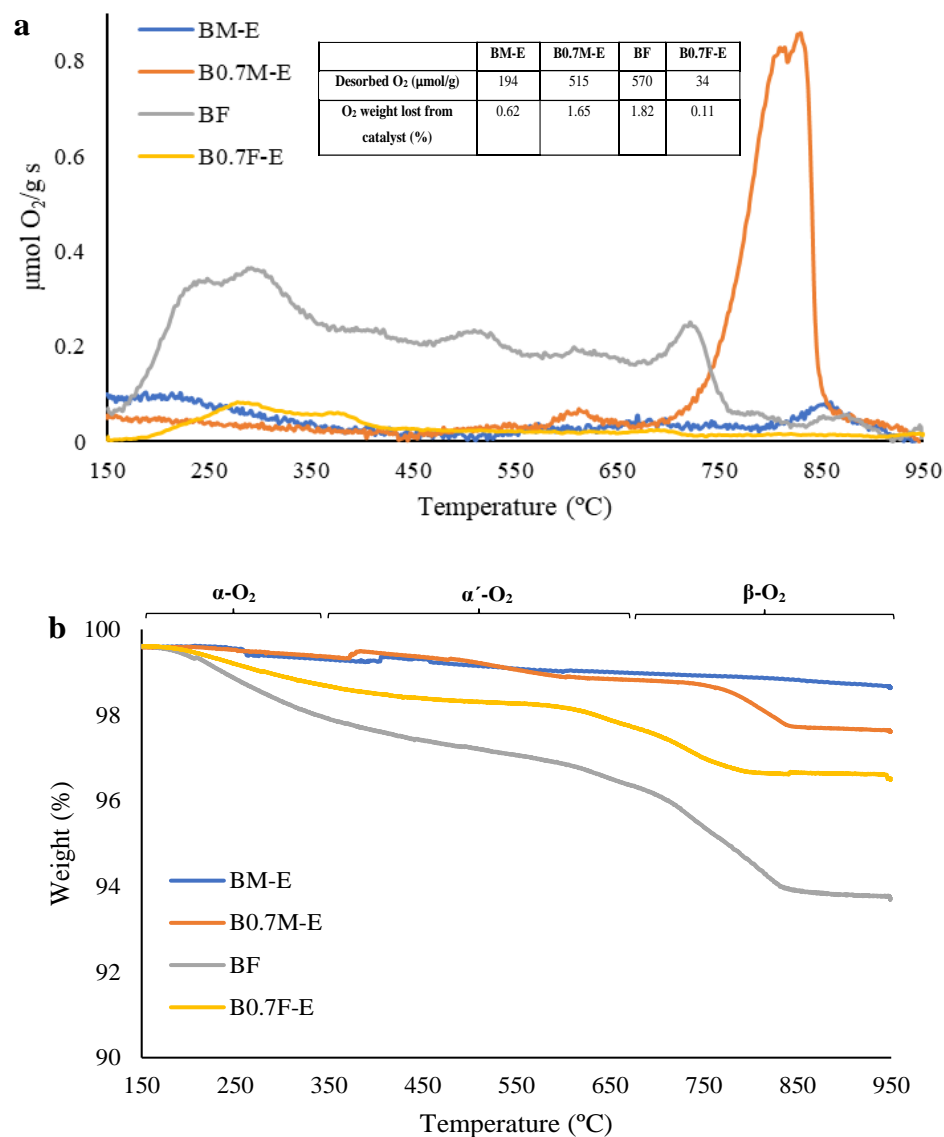


Figure 7. O₂-TPD profiles (a) and weight profiles (b) of catalysts.

Figure 7b shows the weight loss profiles registered during O₂-TPD experiments for the two series of catalysts. Different contributions are identified: (i) below 150 °C, the weight loss is due to the release of chemisorbed water; (ii) from 150 °C to 450 °C, the α -O₂ species are mainly released; (iii) from 650 °C to 850 °C, α' -O₂ and β -O₂ are emitted; and finally, (iv) at approximately 815 °C, BaCO₃ (previously detected by FT-IR and XPS) decomposition takes place [76]. The weight loss of manganese-based samples due to O₂ release (Figure 7a) matches with the corresponding TGA profiles shown in Figure 7b. However, for iron-based catalysts, a higher total weight loss than that expected according to the evolved O₂ (data shown in Figure 7a) is detected due to the decomposition of carbonate groups present in a higher amount in iron-based samples than in manganese-based samples (see XPS and IR results).

2.5. Catalytic Activity

The effect of decreasing the Ba content on the catalytic performance of BM and BF perovskites for CO and soot oxidation in simulated GDI engine exhaust conditions was analyzed.

Figure 8 features the CO conversion profiles for the two tested reaction atmospheres, and Table 4 presents the temperature at which 50% of CO conversion was reached ($T_{50\%}$ values). The CO conversion profiles reveal that all catalysts are active for CO oxidation under the tested conditions, as CO is not oxidized in the absence of a catalyst. However, all catalysts are less active than the 1% Pt/Al₂O₃ used as reference catalyst.

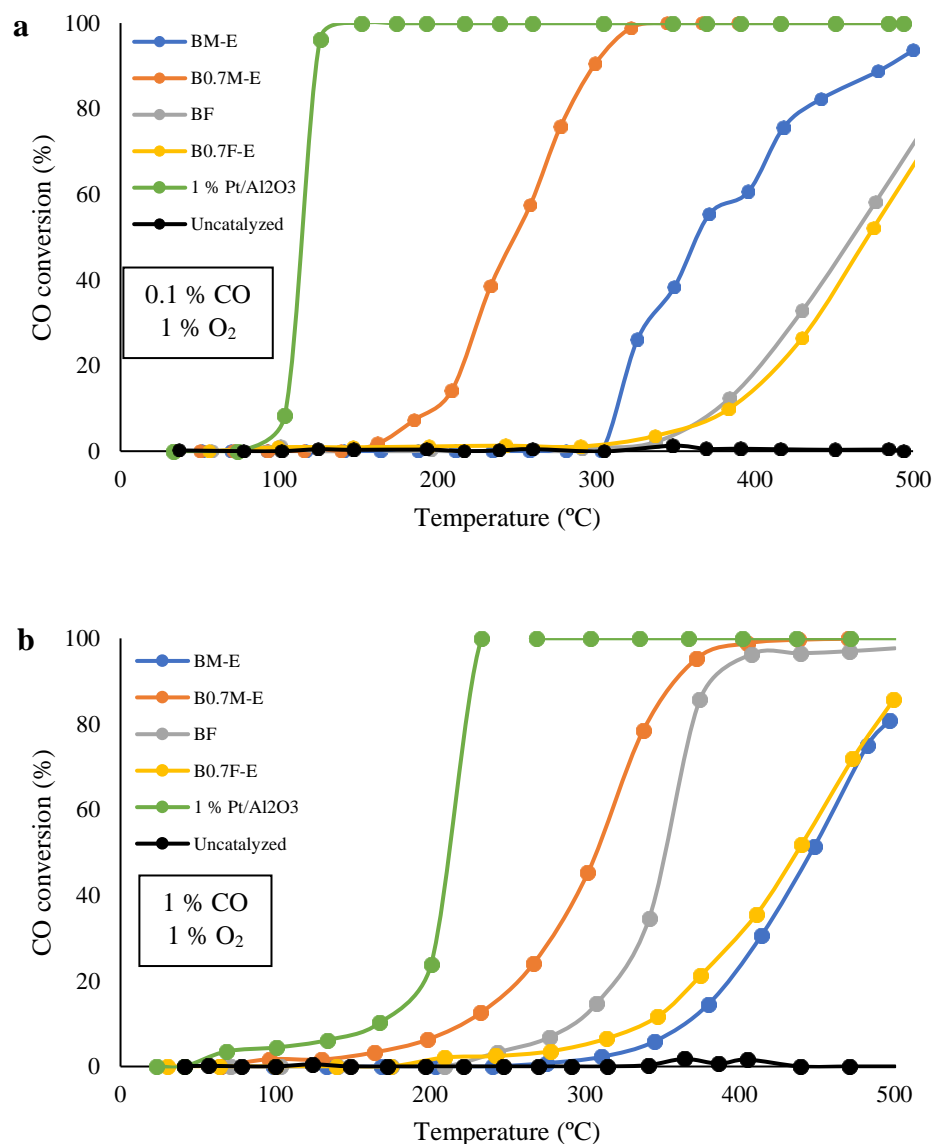


Figure 8. CO conversion profiles (CO-TPR) for the catalysts in 0.1% CO, 1% O₂ in He (a) and 1% CO, 1% O₂ in He (b).

For the low CO content gaseous mixture (0.1% CO, 1% O₂), Figure 8a indicates that manganese-based catalysts are more active than the iron-based catalysts, as Mn is more efficient than Fe in terms of promoting redox processes due to a greater redox versatility [77]. Note that for manganese-based samples, Ba deficiency improves CO conversion at low temperatures, since the B0.7M-E catalyst presents a higher amount of oxygen vacancies (that are active sites for the reaction), a higher amount of Mn(IV), and a higher reducibility than BM-E perovskite. On the contrary, almost no effect of Ba deficiency is detected for iron-based samples because a structural change from perovskite to spinel occurs in this

sample instead of an increase in the amount of oxygen vacancies and/or in the amount of Fe(IV). In fact, B0.7F-E presents a higher $T_{50\%}$ value than BF (see Table 4), suggesting that a spinel structure, which is the main crystalline phase for B0.7F-E, is less active than a perovskite structure for the CO oxidation reaction because of its lower amount of oxygen vacancies and Fe(IV) with respect to BF with a perovskite structure (see XPS and H₂-TPR data in Table 3 and Figures 5b and 6) [78].

Table 4. $T_{50\%}$ values for the tested catalysts and $T_{50\%}$ change ($\Delta T_{50\%}$) in low CO content mixture (0.1% CO, 1% O₂) with respect to the stoichiometric mixture (1% CO, 1% O₂).

Catalyst	$T_{50\%}$ (0.1% CO, 1% O ₂) (°C)	$T_{50\%}$ (1% CO, 1% O ₂) (°C)	$\Delta T_{50\%}$ (°C)
BM-E	364	446	82
B0.7M-E	249	307	58
BF	461	352	−109
B0.7F-E	471	437	−34
1% Pt/Al ₂ O ₃	114	212	98

On the other hand, for a stoichiometric gaseous reactant mixture (1% CO, 1% O₂), Figure 8b shows that the B0.7M-E sample is more active than the BF sample. Therefore, manganese-based mixed oxides with perovskite structures are more active than iron-based mixed oxides with perovskite structures (BF) for CO oxidation under the two tested conditions. This is because manganese-based perovskite presents a higher amount of active sites for CO oxidation than iron-based perovskite, as it presents not only a high fraction of Mn(IV) but also a higher amount of oxygen vacancies. Therefore, it is confirmed that the nature of the B cation in perovskite determines the catalytic performance in oxidation reactions. In this sense, it is well known that electronic configuration of the B cation in perovskite is a key factor for adsorption/activation of reactants (CO and O₂ in this case). In fact, the occupancy of the e_g orbital (which presents the ideal geometry for interacting with the molecular orbitals of CO and O₂ molecules) establishes the adsorption/desorption energy of reactants [79], as the energy of adsorption increases as the number of electrons in the e_g orbital decreases. Therefore, as Fe(III) has two e_g electrons but Mn(III) has only one (and Mn(IV) presents an empty e_g orbital), the CO adsorption energy is higher for manganese perovskites than for iron perovskites. Consequently, manganese allows a more efficient CO activation on the catalyst surface, promoting Langmuir–Hinshelwood (LH) and Eley–Rideal (ER) mechanisms. Additionally, as the amount of oxygen vacancies is higher for manganese perovskites than for iron perovskite, a higher number of active sites is present in the former samples. Note that the prevalence of LH or ER mechanisms mainly depends on the gas mixture composition [59].

Additionally, the data presented in Table 4 shows that the increase in the CO partial pressure has a different effect for manganese than for iron-based samples, i.e., the CO conversion decreases for the former but improves for the latter. The observed decrease in the catalytic activity for manganese-based samples indicates that the higher demand of active sites at higher reactant partial pressure only seems to be achieved at higher temperatures. On the other hand, the increase in the CO conversion at higher CO partial pressures observed for the BF catalyst reveals the participation of α -O₂ and α' -O₂ present (detected during O₂-TPD experiments, see Figure 7a) as active species. In fact, the amount of oxygen evolved by BF and B0.7F-E samples at temperatures below 700 °C (included in Figure 7a) is in agreement with the $\Delta T_{50\%}$ values presented in Table 4. Finally, by comparing $\Delta T_{50\%}$ for B0.7M-E and B0.7F-E catalysts with that observed for the 1% Pt/Al₂O₃ reference sample, it seems that mixed oxide catalysts are more stable than Pt-based catalysts against fluctuations in the composition of the reactant mixture, so they are more resistant to changes in the amount of O₂ and CO in the exhaust evolved by GDI engines, which seems to be an advantage for a potential application.

The soot conversion profiles obtained during the soot oxidation experiments carried out under the simulated conditions close to those of GDI engine exhaust, i.e., an inert atmosphere and a 1% O₂/He gas mixture, are featured in Figure 9a,b. T_{25%}, T_{50%} (temperatures required to achieve the 25% and the 50% of soot conversion, respectively) and the selectivity to CO₂ are featured in Table 5. The data confirm that the two types of catalysts are also able to increase the soot conversion in the two tested atmospheres, as soot oxidation takes place at temperatures lower than for an uncatalyzed reaction. However, the improvement in the soot conversion is lower than that observed for the CO oxidation reaction, being the increase in the selectivity to CO₂ more relevant than the decrease in T_{25%} and T_{50%} values.

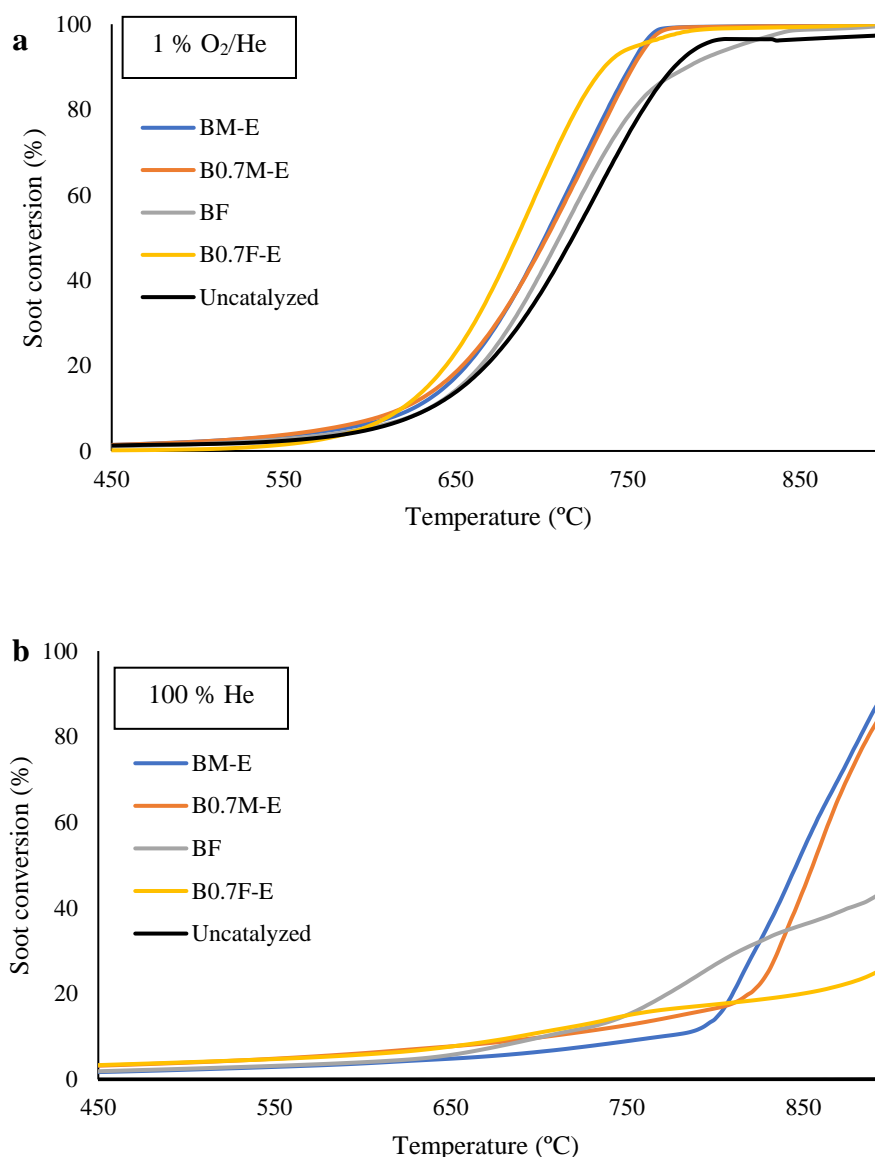


Figure 9. Soot conversion profiles (soot-TPR) for the catalysts in 1% O₂ in He (a) and in 100% He (b).

In 1% O₂/He, the B0.7F-E sample presents the lowest T_{50%} value, so it seems that the spinel structure of B0.7F-E catalysts presents a higher ability to adsorb and dissociate O₂ from the gas phase than a perovskite structure [80].

In the absence of oxygen, as expected [43,81,82], all catalysts show lower soot conversions due to the lower amount of oxygen available (which only comes from the samples). Under these conditions, the BF sample shows the lowest T_{25%}, as it evolves the highest amount of low and intermediate oxygen species (α -O₂ and α' -O₂; see Figure 7a) able to oxidize the soot. However, at temperatures higher than around 800 °C, the conversion in

the presence of manganese notably increases, and, consequently, lower $T_{50\%}$ values are shown for manganese-based samples than for iron-based samples. This behavior seems to be related to the higher emission of β -O₂ able to oxidize soot.

Table 5. $T_{25\%}$, $T_{50\%}$, and selectivity to CO₂ (S_{CO_2}) values for BM-E, B0.7M-E, BF, and B0.7F-E catalysts.

Catalyst	1% O ₂ /He			100% He		
	$T_{25\%}$ (°C)	$T_{50\%}$ (°C)	S_{CO_2} (%)	$T_{25\%}$ (°C)	$T_{50\%}$ (°C)	S_{CO_2} (%)
BM-E	666	701	67	816	847	8
B0.7M-E	665	702	78	830	855	11
BF	674	710	71	794	-	42
B0.7F-E	653	686	63	892	-	33
Uncatalyzed	679	718	42	-	-	-

On the other hand, the selectivity to CO₂ values shown in Table 5 reveal that the generation of CO₂ is highly dependent on the catalyst and on the atmospheric composition. As expected [43,80], the selectivity values in the presence of oxygen in the reaction atmosphere are higher than in inert atmosphere, as in the latter, less oxygen is available for the oxidation of soot. Note that in the presence of O₂, the increase in the selectivity to CO₂ is higher for manganese than for iron-based samples. This is in agreement with the higher ability of Mn with respect to Fe to catalyze the CO oxidation to CO₂, as previously discussed. Finally, it is remarkable that in an inert atmosphere, the Fe based catalysts present a higher selectivity to CO₂ than Mn-based catalysts because the latter metal promotes soot oxidation at higher temperatures, at which CO is the main product of carbon (soot) oxidation [83].

Thus, it can be concluded that the role of Ba_xBO₃ samples as catalysts in oxidation reactions depends on the reaction (CO or soot oxidation) and on the nature of the B cation, as Mn-based are samples more active for CO oxidation, with B0.7F-E showing a higher increase in soot conversion in the presence of oxygen, even though the catalytic effect is more significant for the CO oxidation reaction. Additionally, it has been observed that the decrease in the Ba content improves the catalytic performance of both catalysts, as B0.7M-E is more active than BM-E for the catalysis of CO oxidation, as B0.7F-E is a better catalyst than BF for soot conversion under simulated GDI engine exhaust conditions. This shows that the composition of BaBO₃ mixed oxides can be tailored as a function of the oxidation reaction that has to be catalyzed.

Finally, considering that the four samples studied present a moderate ability as catalysts for CO and soot oxidation compared with other noble-metal-free catalysts [83–85], further optimization of perovskite composition is mandatory. In this sense, it is well known that copper plays an important role as an active phase during CO and soot oxidation reactions [84–86]. Consequently, the next step will be the analysis of the effect of the decrease in the barium content in copper–manganese perovskites [73].

3. Materials and Methods

3.1. Synthesis and Characterization of Catalysts

The Ba_xMnO₃ and Ba_xFeO₃ perovskites were synthesized by employing the sol–gel method adapted to aqueous medium [80,87]. First of all, a 40 mL solution (containing EDTA as a chelating agent in a 1:2 molar Mn/Fe:EDTA ratio) was prepared at 60 °C. Ba(NO₃)₂ was added as a Ba precursor; then, Mn(NO₃)₂·4 H₂O or Fe(NO₃)₃·9 H₂O was included as an Mn or Fe precursor, respectively. After that, citric acid was incorporated using a 1:2, Mn(Fe):citric acid molar ratio. Subsequently, the temperature was increased to 80 °C to assure gel formation. The described procedure was carried out keeping the pH at 9 using an ammonia solution (30% wt). Finally, the obtained gel was dried at 150 °C for 12 h, and as the last step, the solid was calcinated at 850 °C for 6 h. Additionally, in an attempt to decrease the number of crystalline phases present in the samples, Ba_xFeO₃ catalysts were synthesized using the same method but avoiding the use of EDTA (named BF and B0.7F).

Thus, even though the synthesis method was the same, some experimental variables were slightly modified with respect to the procedure described above: (i) citric acid was dissolved in a 1:2 molar Mn (Fe):citric acid ratio before adding the metal precursors, (ii) barium acetate was used instead of barium nitrate, (iii) the gelation process was conducted at 65 °C, and (iv) the drying process was carried out at 90 °C for 48 h.

For sample characterization, the following techniques were employed.

The chemical bulk composition was analyzed by μ -XRF on an Orbis EDAX analyzer.

The textural properties were determined by N₂ adsorption at −196 °C using an Autosorb-6B instrument from Quantachrome (Anton Paar Austria GmbH). The samples were degassed at 250 °C for 4 h before the N₂ adsorption experiments.

The crystalline structure was obtained using X-ray diffraction (XRD). The X-ray patterns were recorded between 20° and 80° 2 θ angles with a step rate of 0.4°/min and using Cu K α (0.15418 nm) radiation in a Bruker D8-Advance device. FT-IR spectra from 4000 to 500 cm^{−1} were also obtained using a BRUKER IFS 66/S apparatus with a spectral resolution of 4 cm^{−1}.

Surface chemistry was studied by X-ray photoelectron spectroscopy (XPS) using a K-Alpha photoelectron spectrometer by Thermo-Scientific with an Al K α (1486.7 eV) radiation source. To obtain XPS spectra, the pressure of the analysis chamber was maintained at 5 × 10^{−10} mbar. The binding energy (BE) and kinetic energy (KE) scales were adjusted by setting the C 1s transition to 284.6 eV, and the BE and KE values were determined with the peak-fit software of the spectrometer. The O_L/(Ba + Mn/Fe), Mn(IV)/Mn(III), and Fe(IV)/Fe(III) XPS ratios were calculated using the area under the suggested deconvoluted bands of O 1s, Mn 2p^{3/2}, Fe 2p^{3/2}, and Ba 3d^{5/2}.

The reducibility of catalysts was determined by temperature-programmed reduction with H₂ (H₂-TPR) in a Pulse Chemisorb 2705 (from Micromeritics) provided by a thermal conductivity detector (TCD) and using 30 mg of sample heated at 10 °C/min from 25 °C to 1000 °C in a 5% H₂/Ar atmosphere (40 mL/min). Quantification of the H₂ consumption was carried out using a CuO reference sample.

O₂-TPD experiments were performed in a TG-MS (Q-600-TA and Thermostar from Balzers Instruments (Pfeiffer Vacuum GmbH, Germany), respectively) with 16 mg of sample heated at 10 °C/min from room temperature to 950 °C under a 100 mL/min helium atmosphere. Moreover, all the samples were preheated to 150 °C for 1 h for moisture removal. The 18, 28, 32, and 44 m/z signals were registered for the H₂O, CO, O₂, and CO₂ evolved during the experiments, respectively. The amount of evolved oxygen was estimated using a CuO reference sample, and the weight data recorded by the TG system were used to obtain the mass loss profiles.

3.2. Activity Tests

To determine the catalytic activity for CO oxidation, temperature-programmed reaction (CO-TPR) experiments were developed using two reactant mixtures composed of (i) 0.1% CO and 1% O₂ in He (low CO reactant mixture) and (ii) 1% CO and 1% O₂ in He (near-stoichiometric reactant mixture, which simulates the actual working conditions of GDI engines). For the experiments, 50 mg of catalysts and 100 mg of SiC were loaded into a U-shaped quartz reactor, and a 10 °C/min heating rate was used from room temperature to 500 °C. The mixture catalyst-SiC was preheated for 1 h at 600 °C in a 5% O₂/He gas mixture in order to clean the surface of the catalysts. For quantification of reaction products, a HP6890 gas chromatograph equipped with a thermal conductivity detector and two packed columns (Porapack-Q and MolSieve-13X) was employed.

The CO conversion was determined using the following equation.

$$\text{CO conversion (\%)} = ((\text{CO}_{\text{in}} - \text{CO}_{\text{out}})/\text{CO}_{\text{in}}) \cdot 100 \quad (1)$$

The catalytic tests for the soot oxidation reaction under simulated GDI conditions were performed in the TG-MS system used for O₂-TPD experiments. To develop these tests, 16 mg of a catalyst and soot mixture (soot:catalyst ratio of 1:8, using Printex-U as model

soot in loose contact mode) was preheated for 1 h at 150 °C in a 1% O₂/He gas mixture (100 mL/min); then, the temperature was increased at 10 °C/min until 900 °C (soot-TPR). Two different reactant atmospheres were employed: (i) 1% O₂/He, which simulates “fuel cuts” GDI exhaust conditions, and (ii) 100% He, which reproduces regular stoichiometric GDI operations [43].

Soot conversion and the selectivity to CO₂ were estimated using the following equations:

$$\text{Soot conversion (\%)} = ((\Sigma_0^t(\text{CO}_2 + \text{CO}))/\Sigma_0^{\text{final}}(\text{CO}_2 + \text{CO})) \cdot 100 \quad (2)$$

$$\text{Selectivity to CO}_2 \text{ (\%)} = (\text{CO}_{2,\text{total}}/\Sigma_0^{\text{final}}(\text{CO}_2 + \text{CO})) \cdot 100 \quad (3)$$

where $\Sigma_0^t(\text{CO}_2 + \text{CO})$ is the amount of CO₂ and CO evolved at time t, while $\Sigma_0^{\text{final}}(\text{CO}_2 + \text{CO})$ is the total amount of CO + CO₂ evolved during the test coming from the oxidation of the total amount of soot.

4. Conclusions

In this study, two series of Ba_xMnO₃ and Ba_xFeO₃ (x = 1 and 0.7) catalysts were synthesized, characterized, and tested for CO and soot oxidation reactions under simulated GDI exhaust conditions. Based on the results discussed above, the following conclusions can be exposed:

- (1) Manganese-based samples present a BaMnO₃ hexagonal perovskite structure, as the decrease in the amount of Ba does not significantly modify the crystalline structure. For iron-based samples, the decrease in the Ba content promotes the transition from a BaFeO_{2.67} hexagonal perovskite structure to a BaFe₂O₄ spinel structure.
- (2) To compensate for the Ba deficiency in the manganese-based samples, the amount of Mn(IV) and the oxygen vacancies increases, allowing a higher reducibility and oxygen mobility. In iron-based samples, the Ba deficiency only causes a change in the structure from perovskite to spinel.
- (3) Manganese-based perovskites (BM-E and B0.7M-E) show a better catalytic performance than iron-based perovskite (BF) for CO oxidation reactions due to the higher generation of active sites.
- (4) The decrease in the Ba content improves the catalytic performance of both catalysts, as B0.7M-E is more active than BM-E for CO oxidation, and B0.7F-E presents a higher activity for soot conversion than BF under simulated GDI engine exhaust conditions. This shows that the composition of BaBO₃ mixed oxides can be tailored as function of the oxidation reaction to be catalyzed.

Author Contributions: The individual contributions of each author are indicated as follows: Á.D.-V.: investigation, resources, data curation, and writing—original draft preparation); S.M.-V.: investigation and resources; V.T.-R.: investigation and resources; and M.-J.I.-G.: conceptualization, methodology, writing—review and editing, visualization, supervision, project administration, and funding acquisition. All authors have read and agreed to the published version of the manuscript.

Funding: This research was funded by the Spanish Government (MINCINN: PID2019-105542RB-I00/AEI/10.13039/501100011033 Project), the European Union (FEDER Funds), and Generalitat Valenciana (CIPROM/2021-070 Project).

Institutional Review Board Statement: Not applicable.

Informed Consent Statement: Not applicable.

Data Availability Statement: Not applicable.

Conflicts of Interest: The authors declare no conflict of interest.

References

1. Thornton, P.K.; Ericksen, P.J.; Herrero, M.; Challinor, A.J. Climate variability and vulnerability to climate change: A review. *Glob. Chang. Biol.* **2014**, *20*, 3313–3328. [[CrossRef](#)]
2. VijayaVenkataRaman, S.; Iniyar, S.; Goic, R. A review of climate change, mitigation and adaptation. *Renew. Sustain. Energy Rev.* **2012**, *16*, 878–897. [[CrossRef](#)]
3. Liu, D.; Yang, D.; Huang, A. LEAP-based greenhouse gases emissions peak and low carbon pathways in China's tourist industry. *Int. J. Environ. Res. Public Health* **2021**, *18*, 1218. [[CrossRef](#)] [[PubMed](#)]
4. Massar, M.; Reza, I.; Rahman, S.M.; Abdullah, S.M.H.; Jamal, A.; Al-Ismael, F.S. Impacts of autonomous vehicles on greenhouse gas emissions—Positive or negative? *Int. J. Environ. Res. Public Health* **2021**, *18*, 5567. [[CrossRef](#)]
5. Rajper, S.Z.; Albrecht, J. Prospects of electric vehicles in the developing countries: A literature review. *Sustainability* **2020**, *12*, 1906. [[CrossRef](#)]
6. Richardson, D.B. Electric vehicles and the electric grid: A review of modelling approaches, impacts, and renewable energy integration. *Renew. Sustain. Energy Rev.* **2013**, *19*, 247–254. [[CrossRef](#)]
7. Dolganova, I.; Rödl, A.; Bach, V.; Kaltschmitt, M.; Finkbeiner, M. A review of life cycle assessment studies of electric vehicles with a focus on resource use. *Resources* **2020**, *9*, 32. [[CrossRef](#)]
8. Pollet, B.G.; Staffell, I.; Shang, J.L. Current status of hybrid, battery and fuel cell electric vehicles: From electrochemistry to market prospects. *Electrochim. Acta* **2012**, *84*, 235–249. [[CrossRef](#)]
9. Tran, M.K.; Bhatti, A.; Vrolyk, R.; Wong, D.; Panchal, S.; Fowler, M.; Fraser, R. A review of range extenders in battery electric vehicles: Current progress and future perspectives. *World Electr. Veh. J.* **2021**, *12*, 54. [[CrossRef](#)]
10. Liang, H.; Jin, B.; Li, M.; Yuan, X.; Wan, J.; Liu, W.; Wu, X.; Liu, S. Highly reactive and thermally stable Ag/YSZ catalysts with microporous fiber-like morphology for soot combustion. *Appl. Catal. B Environ.* **2021**, *294*, 120271. [[CrossRef](#)]
11. Zhao, Z.; Ma, J.; Li, M.; Liu, W.; Wu, X.; Liu, S. Model Ag/CeO₂ catalysts for soot combustion: Roles of silver species and catalyst stability. *Chem. Eng. J.* **2022**, *430*, 132802. [[CrossRef](#)]
12. Matarrese, R. Catalytic materials for gasoline particulate filters soot oxidation. *Catalysts* **2021**, *11*, 890. [[CrossRef](#)]
13. Grabchenko, M.V.; Mikheeva, N.N.; Mamontov, G.V.; Salaev, M.A.; Liotta, L.F.; Vodyankina, O.V. Ag/CeO₂ composites for catalytic abatement of CO, soot and VOCs. *Catalysts* **2018**, *8*, 285. [[CrossRef](#)]
14. Wang, J.A.; González, G.; Chen, L.; Valenzuela, M.A.; Moran-Pineda, M.; Vázquez, A.; Castillo, S. Templated synthesis and catalytic properties of an Rh/ceria-zirconia catalyst. *React. Kinet. Catal. Lett.* **2007**, *90*, 381–387. [[CrossRef](#)]
15. Bernal, S.; Blanco, G.; Cauqui, M.A.; Corchado, P.; Pintado, J.M.; Rodríguez-Izquierdo, J.M.; Vidal, H. Fundamental properties of a new cerium-based mixed oxide alternative as TWC component. *Stud. Surf. Sci. Catal.* **1998**, *116*, 611–618.
16. Peña, M.A.; Fierro, J.L.G. Chemical structures and performance of perovskite oxides. *Chem. Rev.* **2001**, *101*, 1981–2018. [[CrossRef](#)] [[PubMed](#)]
17. Yadav, P.; Yadav, S.; Atri, S.; Tomar, R. A brief review on key role of perovskite oxides as catalyst. *Chem. Sel.* **2021**, *6*, 12947–12959. [[CrossRef](#)]
18. Wang, K.; Han, C.; Shao, Z.; Qiu, J.; Wang, S.; Liu, S. Perovskite oxide catalysts for advanced oxidation reactions. *Adv. Funct. Mater.* **2021**, *31*, 2102089. [[CrossRef](#)]
19. Peron, G.; Glisenti, A. Perovskites as alternatives to noble metals in automotive exhaust abatement: Activation of oxygen on LaCrO₃ and LaMnO₃. *Top. Catal.* **2018**, *62*, 244–251. [[CrossRef](#)]
20. Barbero, B.P.; Gamboa, J.A.; Cadús, L.E. Synthesis and characterization of La_{1-x}Ca_xFeO₃ perovskite-type oxide catalysts for total oxidation of volatile organic compounds. *Appl. Catal. B Environ.* **2006**, *65*, 21–30. [[CrossRef](#)]
21. Cant, N.W.; Angove, D.E. The origin of apparent deactivation during the oxidation of carbon monoxide over silica-supported platinum at moderate temperatures. *J. Catal.* **1986**, *97*, 36–42. [[CrossRef](#)]
22. Royer, S.; Duprez, D. Catalytic oxidation of carbon monoxide over transition metal oxides. *ChemCatChem* **2011**, *3*, 24–65. [[CrossRef](#)]
23. Voorhoeve, R.J.H.; Johnson, D.W.; Remeika, J.P.; Gallagher, P.K. Perovskite oxides: Materials science in catalysis. *Science* **1977**, *195*, 827–833. [[CrossRef](#)] [[PubMed](#)]
24. Atkins, P.W.; Overton, T.; Rourke, J.; Weller, M.; Armstrong, F.; Hagerman, M. *Shriver & Atkins' Inorganic Chemistry*, 5th ed.; Oxford University Press: Oxford, UK, 2010; p. 541.
25. Voorhoeve, R.J.H. *Perovskite-Related Oxides as Oxidation-Reduction Catalysts*, 1st ed.; Academic Press Inc.: Cambridge, MA, USA, 1977; pp. 129–180.
26. Tascón, J.M.D.; González-Tejuca, L. Catalytic activity of perovskite-type oxides LaMeO₃. *React. Kinet. Catal. Lett.* **1980**, *15*, 185–191. [[CrossRef](#)]
27. Prasad, R.; Singh, P. A review on CO oxidation over copper chromite catalyst. *Catal. Rev. Sci. Eng.* **2012**, *54*, 224–279. [[CrossRef](#)]
28. Pinto, D.; Glisenti, A. Pulsed reactivity on LaCoO₃-based perovskites: A comprehensive approach to elucidate the CO oxidation mechanism and the effect of dopants. *Catal. Sci. Technol.* **2019**, *9*, 2749–2757. [[CrossRef](#)]
29. Ouyang, X.; Scott, S.L. Mechanism for CO oxidation catalyzed by Pd-substituted BaCeO₃, and the local structure of active sites. *J. Catal.* **2010**, *273*, 83–91. [[CrossRef](#)]

30. Najjar, H.; Lamonier, J.F.; Mentré, O.; Giraudon, J.M. Optimization of the combustion synthesis towards efficient LaMnO_{3+y} catalysts in methane oxidation. *Appl. Catal. B Environ.* **2011**, *106*, 149–159. [CrossRef]
31. Zhang, C.; Wang, C.; Hua, W.; Guo, Y.; Lu, G.; Gil, S.; Giroir-Fendler, A. Relationship between catalytic deactivation and physicochemical properties of LaMnO_3 perovskite catalyst during catalytic oxidation of vinyl chloride. *Appl. Catal. B Environ.* **2016**, *186*, 173–183. [CrossRef]
32. Merino, N.A.; Barbero, B.P.; Eloy, P.; Cadús, L.E. $\text{La}_{1-x}\text{Ca}_x\text{CoO}_3$ perovskite-type oxides: Identification of the surface oxygen species by XPS. *Appl. Surf. Sci.* **2006**, *253*, 1489–1493. [CrossRef]
33. Buciuman, F.C.; Patcas, F.; Zsako, J. TPR-study of substitution effects on reducibility and oxidative non-stoichiometry of $\text{La}_{0.8}\text{A}'_{0.2}\text{MnO}_{3+\delta}$ perovskites. *J. Therm. Anal. Calorim.* **2000**, *61*, 819–825. [CrossRef]
34. Patcas, F.; Buciuman, F.C.; Zsako, J. Oxygen non-stoichiometry and reducibility of B-site substituted lanthanum manganites. *Thermochim. Acta* **2000**, *360*, 71–76. [CrossRef]
35. Irusta, S.; Pina, M.P.; Menéndez, M.; Santamaría, J. Catalytic combustion of volatile organic compounds over La-based perovskites. *J. Catal.* **1998**, *179*, 400–412. [CrossRef]
36. Torregrosa-Rivero, V.; Sánchez-Adsuar, M.S.; Illán-Gómez, M.J. Modified BaMnO_3 -based catalysts for gasoline particle filters (GPF): A preliminary study. *Catalysts* **2022**, *12*, 1325. [CrossRef]
37. Torregrosa-Rivero, V.; Sánchez-Adsuar, M.S.; Illán-Gómez, M.J. Exploring the effect of using carbon black in the sol-gel synthesis of BaMnO_3 and $\text{BaMn}_{0.7}\text{Cu}_{0.3}\text{O}_3$ perovskite catalysts for CO oxidation. *Catal. Today* **2023**. [CrossRef]
38. Díaz-Verde, A.; Torregrosa-Rivero, V.; Sánchez-Adsuar, M.S.; Illán-Gómez, M.J. In Catalizadores basados en Ba_xMnO_3 para la oxidación de CO. In Proceedings of the IV Encuentro de Jóvenes Investigadores de la SECAT, Bilbao, Spain, 21–23 September 2020.
39. Li, S.; Bergman, B. Doping effect on secondary phases, microstructure and electrical conductivities of LaGaO_3 based perovskites. *J. Eur. Ceram. Soc.* **2009**, *29*, 1139–1146. [CrossRef]
40. Sun, M.; Jiang, Y.; Li, F.; Xia, M.; Xue, B.; Liu, D. Structure, dye degradation activity and stability of oxygen defective BaFeO_{3-x} . *Mater. Trans.* **2010**, *51*, 1981–1989. [CrossRef]
41. Islam, S.A.U.; Ikram, M. Structural stability improvement, Williamson Hall analysis and band-gap tailoring through A-site Sr doping in rare earth based double perovskite $\text{La}_2\text{NiMnO}_6$. *Rare Met.* **2019**, *38*, 805–813. [CrossRef]
42. Cimino, S.; Lisi, L.; De Rossi, S.; Faticanti, M.; Porta, P. Methane combustion and CO oxidation on $\text{LaAl}_{1-x}\text{Mn}_x\text{O}_3$ perovskite-type oxide solid solutions. *Appl. Catal. B* **2003**, *43*, 397–406. [CrossRef]
43. Torregrosa-Rivero, V.; Moreno-Marcos, C.; Albaladejo-Fuentes, V.; Sánchez-Adsuar, M.S.; Illán-Gómez, M.J. $\text{BaFe}_{1-x}\text{Cu}_x\text{O}_3$ perovskites as active phase for diesel (DPF) and gasoline particle filters (GPF). *Nanomaterials* **2019**, *9*, 1551. [CrossRef] [PubMed]
44. Hu, Y.; Han, X.; Zhao, Q.; Du, J.; Cheng, F.; Chen, J. Porous perovskite calcium-manganese oxide microspheres as an efficient catalyst for rechargeable sodium-oxygen batteries. *J. Mater. Chem. A.* **2015**, *3*, 3320–3324. [CrossRef]
45. Xu, H.; Gao, L.; Guo, J. Preparation and characterizations of tetragonal barium titanate powders by hydrothermal method. *J. Eur. Ceram. Soc.* **2002**, *22*, 1163–1170. [CrossRef]
46. Balamurugan, S.; Asha, M.K.S.; Gokul, R.T.S.; Parthiban, P. Mechano-thermal synthesis and characterization of BaMnO_3 nano-needles. *J. Nanosci. Nanotechnol.* **2015**, *15*, 5978–5986. [CrossRef]
47. Gao, F.; Lewis, R.A.; Wang, X.L.; Dou, S.X. Far-infrared reflection and transmission of $\text{La}_{1-x}\text{Ca}_x\text{MnO}_3$. *J. Alloys Compd.* **2002**, *347*, 314–318. [CrossRef]
48. Roy, C.; Budhani, R.C. Raman- and infrared-active phonons in hexagonal BaMnO_3 . *Phys. Rev. B* **1998**, *58*, 8174–8177. [CrossRef]
49. Xian, H.; Zhang, X.; Li, X.; Zou, H.; Meng, M.; Zou, Z.; Guo, L.; Tsubaki, N. Effect of the calcination conditions on the NO_x storage behavior of the perovskite BaFeO_{3-x} catalysts. *Catal. Today* **2010**, *158*, 215–219. [CrossRef]
50. Yang, Y.; Jiang, Y.; Wang, Y.; Sun, Y. Photoinduced decomposition of BaFeO_3 during photodegradation of methyl orange. *J. Mol. Catal. A Chem.* **2007**, *270*, 56–60. [CrossRef]
51. Singh, H.; Rajput, J.K. Novel perovskite nanocatalyst (BiFeO_3) for the photodegradation of rhodamine B/tartrazine and swift reduction of nitro compounds. *J. Iran. Chem. Soc.* **2019**, *16*, 2409–2432. [CrossRef]
52. Singh, H.; Garg, N.; Arora, P.; Rajput, J.K.; Jigyasa. Sucrose chelated auto combustion synthesis of BiFeO_3 nanoparticles: Magnetically recoverable catalyst for the one-pot synthesis of polyhydroquinoline. *Appl. Organomet. Chem.* **2018**, *32*, e4357. [CrossRef]
53. Fang, Z.; Jiang, H.; Gong, J.; Zhang, H.; Hu, X.; Ouyang, K.; Guo, Y.; Hu, X.; Wang, H.; Wang, P. Removal of tetracycline hydrochloride from water by visible-light photocatalysis using BiFeO_3/BC materials. *Catalysts* **2022**, *12*, 1461. [CrossRef]
54. X-ray Photoelectron Spectroscopy Learning Center. Available online: <https://www.thermofisher.com/es/es/home/materials-science/learning-center/surface-analysis.html> (accessed on 10 December 2022).
55. Quiñonez-Ortiz, J.L.; García-González, L.; Cancino-Gordillo, F.E.; Pal, U. Particle dispersion and lattice distortion induced magnetic behavior of $\text{La}_{1-x}\text{Sr}_x\text{MnO}_3$ perovskite nanoparticles grown by salt-assisted solid-state synthesis. *Mater. Chem. Phys.* **2020**, *246*, 122834. [CrossRef]
56. Ghaffari, M.; Shannon, M.; Hui, H.; Tan, O.K.; Irannejad, A. Preparation, surface state and band structure studies of $\text{SrTi}_{(1-x)}\text{Fe}_{(x)}\text{O}_{(3-\delta)}$ ($x = 0-1$) perovskite-type nano structure by X-ray and ultraviolet photoelectron spectroscopy. *Surf. Sci.* **2012**, *606*, 670–677. [CrossRef]

57. Hona, R.K.; Ramezanipour, F. Disparity in electrical and magnetic properties of isostructural oxygen-deficient perovskites BaSrCo₂O_{6-δ} and BaSrCoFeO_{6-δ}. *J. Mater. Sci. Mater. Electron.* **2018**, *29*, 13464–13473. [CrossRef]
58. Tabata, K.; Hirano, Y.; Suzuki, E. XPS studies on the oxygen species of LaMn_{1-x}Cu_xO_{3+λ}. *Appl. Catal. A Gen.* **1998**, *170*, 245–254. [CrossRef]
59. Yang, J.; Hu, S.; Fang, Y.; Hoang, S.; Li, L.; Yang, W.; Liang, Z.; Wu, J.; Hu, J.; Xiao, W.; et al. Oxygen vacancy promoted O₂ activation over perovskite oxide for low-temperature CO oxidation. *ACS Catal.* **2019**, *9*, 9751–9763. [CrossRef]
60. LaSurface Database. Available online: <http://www.lasurface.com/accueil/> (accessed on 13 December 2022).
61. López-Suárez, F.E.; Bueno-López, A.; Illán-Gómez, M.J.; Trawczynski, J. Potassium-copper perovskite catalysts for mild temperature diesel soot combustion. *Appl. Catal. A Gen.* **2014**, *485*, 214–221. [CrossRef]
62. Albaladejo-Fuentes, V.; López-Suárez, F.E.; Sánchez-Adsuar, M.S.; Illán-Gómez, M.J. Tailoring the properties of BaTi_{0.8}Cu_{0.2}O₃ catalyst selecting the synthesis method. *Appl. Catal. A Gen.* **2016**, *519*, 7–15. [CrossRef]
63. Wang, P.; Yao, L.; Wang, M.; Wu, W. XPS and voltammetric studies on La_{1-x}Sr_xCoO_{3-δ} perovskite oxide electrodes. *J. Alloys Compd.* **2000**, *311*, 53–56. [CrossRef]
64. Liu, L.; Sun, J.; Ding, J.; Zhang, Y.; Jia, J.; Sun, T. Catalytic oxidation of VOCs over SmMnO₃ perovskites: Catalyst synthesis, change mechanism of active species, and degradation path of toluene. *Inorg. Chem.* **2019**, *58*, 14275–14283. [CrossRef]
65. Torregrosa-Rivero, V. BaMnO₃ Perovskite-Based Catalysts for Pollution Control Generated by Highly Efficient Automotive Engines. Doctoral Thesis, University of Alicante, San Vicente del Raspeig, Spain, 2021.
66. Liu, Y.; Dai, H.; Du, Y.; Deng, J.; Zhang, L.; Zhao, Z. Lysine-aided PMMA-templating preparation and high performance of three dimensionally ordered microporous LaMnO₃ with mesoporous walls for the catalytic combustion of toluene. *Appl. Catal. B Environ.* **2012**, *119–120*, 20–31. [CrossRef]
67. Shen, M.; Zhao, Z.; Chen, J.; Su, Y.; Wang, J.; Wang, X. Effects of calcium substitute in LaMnO₃ perovskites for NO catalytic oxidation. *J. Rare Earths* **2013**, *31*, 119–123. [CrossRef]
68. Sarshar, Z.; Kaliaguine, S. Reduction kinetics of perovskite-based oxygen carriers for chemical looping combustion. *Ind. Eng. Chem. Res.* **2013**, *52*, 6946–6955. [CrossRef]
69. Sarshar, Z.; Kleitz, F.; Kaliaguine, S. Novel oxygen carriers for chemical looping combustion: La_{1-x}Ce_xBO₃ (B = Co, Mn) perovskites synthesized by reactive grinding and nanocasting. *Energy Environ. Sci.* **2011**, *4*, 4258–4269. [CrossRef]
70. Gao, Z.; Wang, H.; Ma, H.; Li, Z. Preparation and characterization of the non-stoichiometric La-Mn perovskites. *J. Alloys Compd.* **2015**, *646*, 73–79. [CrossRef]
71. Hosseinpour, N.; Mortazavi, Y.; Khodadadi, A.A. Cumene cracking activity and enhanced regeneration of FCC catalysts comprising HY-zeolite and LaBO₃ (B = Co, Mn, and Fe) perovskites. *Appl. Catal. A Gen.* **2014**, *487*, 26–35. [CrossRef]
72. Gan, R.; Nishida, Y.; Haneda, M. Effect of B-site substitution on the catalytic activity of La-based perovskite for oxidative coupling of methane. *Phys. Status Solidi B* **2022**, *259*, 2100544. [CrossRef]
73. Torregrosa-Rivero, V.; Albaladejo-Fuentes, V.; Sánchez-Adsuar, M.S.; Illán-Gómez, M.J. Copper doped BaMnO₃ perovskite catalysts for NO oxidation and NO₂-assisted diesel soot removal. *RSC Adv.* **2017**, *7*, 35228–35238. [CrossRef]
74. Zhu, Y.; Sun, Y.; Niu, X.; Yuan, F.; Fu, H. Preparation of La-Mn-O perovskite catalyst by microwave irradiation method and its application to methane combustion. *Catal. Lett.* **2010**, *135*, 152–158. [CrossRef]
75. Shibata, S.; Kamata, K.; Hara, M. Stability enhancement of iron-based perovskite catalysts by A-site substitution for oxidative transposition of α-bromostyrene to phenacyl bromide. *ChemCatChem* **2022**, *14*, e202200395. [CrossRef]
76. Albaladejo-Fuentes, V.; Sánchez-Adsuar, M.S.; Anderson, J.A.; Illán-Gómez, M.J. NO_x storage on BaTi_{0.8}Cu_{0.2}O₃ perovskite catalysts: Addressing a feasible mechanism. *Nanomaterials* **2021**, *11*, 2133. [CrossRef]
77. Teraoka, Y.; Nii, H.; Kagawa, S.; Jansson, K.; Nygren, M. Influence of the simultaneous substitution of Cu and Ru in the perovskite-type (La, Sr) MO₃ (M = Al, Mn, Fe, Co) on the catalytic activity for CO oxidation and CO-NO reactions. *Appl. Catal. A Gen.* **2000**, *194–195*, 35–41. [CrossRef]
78. Dey, S.; Dhal, G.C. A review of synthesis, structure and applications in hopcalite catalysts for carbon monoxide oxidation. *Aerosol Sci. Eng.* **2019**, *3*, 97–131. [CrossRef]
79. Hwang, J.; Rao, R.R.; Giordano, L.; Katayama, Y.; Yu, Y.; Shao-Horn, Y. Perovskites in catalysis and electrocatalysis. *Science* **2017**, *358*, 751–756. [CrossRef]
80. Campagnoli, E.; Tavares, A.; Fabbrini, L.; Rossetti, I.; Dubitsky, Y.A.; Zaopo, A.; Forni, L. Effect of preparation method on activity and stability of LaMnO₃ and LaCoO₃ catalysts for the flameless combustion of methane. *Appl. Catal. B Environ.* **2005**, *55*, 133–139. [CrossRef]
81. Moreno-Marcos, C.; Torregrosa-Rivero, V.; Albaladejo-Fuentes, V.; Sánchez-Adsuar, M.S.; Illán-Gómez, M.J. BaFe_{1-x}Cu_xO₃ perovskites as soot oxidation catalysts for gasoline particulate filters (GPF): A preliminary study. *Top. Catal.* **2019**, *62*, 413–418. [CrossRef]
82. Martinovic, F.; Galletti, C.; Bensaid, S.; Pirone, R.; Deorsola, A. Soot oxidation in low-O₂ and O₂-free environments by lanthanum-based perovskites: Structural changes and the effect of Ag doping. *Catal. Sci. Technol.* **2022**, *12*, 5453–5464. [CrossRef]
83. Rao, Y.K. *Stoichiometry and Thermodynamics of Metallurgical Processes*; Cambridge University Press: Cambridge, UK, 1985; p. 377.
84. Wan, H.; Wang, Z.; Zhu, J.; Li, X.; Liu, B.; Gao, F.; Dong, L.; Chen, Y. Influence of CO pretreatment on the activities of CuO/γ-Al₂O₃ catalysts in CO + O₂ reaction. *Appl. Catal. B Environ.* **2008**, *79*, 254–261. [CrossRef]

85. Zhou, J.; Pan, J.; Jin, Y.; Peng, Z.; Xu, Z.; Chen, Q.; Ren, P.; Zhou, X.; Wu, K. Single-cation catalyst: Ni cation in monolayered CuO for CO oxidation. *J. Am. Chem. Soc.* **2022**, *144*, 8430–8433. [[CrossRef](#)]
86. Fu, M.; Yue, X.; Ye, D.; Ouyang, J.; Huang, B.; Wu, J.; Liang, H. Soot oxidation via CuO doped CeO₂ catalysts prepared using coprecipitation and citrate acid complex-combustion synthesis. *Catal. Today* **2010**, *153*, 125–132. [[CrossRef](#)]
87. Flores-Lasluisa, J.X.; Huerta, F.; Cazorla-Amorós, D.; Morallón, E. Structural and morphological alterations induced by cobalt substitution in LaMnO₃ perovskites. *J. Colloid Interface Sci.* **2019**, *556*, 658–666. [[CrossRef](#)]

Disclaimer/Publisher’s Note: The statements, opinions and data contained in all publications are solely those of the individual author(s) and contributor(s) and not of MDPI and/or the editor(s). MDPI and/or the editor(s) disclaim responsibility for any injury to people or property resulting from any ideas, methods, instructions or products referred to in the content.